ADVANCED MATERIALS
www.advmat.de

Carbon Nanotube-Directed 7 GPa Heterocyclic Aramid Fiber and Its Application in Artificial Muscles

Dan Yan, Jiajun Luo, Shijun Wang, Xiaocang Han, Xudong Lei, Kun Jiao, Xianqian Wu, Liu Qian, Xinshi Zhang, Xiaoxu Zhao, Jiangtao Di, Zhong Zhang, Zhenfei Gao, and Jin Zhang**

Poly(p-phenylene-benzimidazole-terephthalamide) (PBIA) fibers with excellent mechanical properties are widely used in fields that require impact-resistant materials such as ballistic protection and aerospace. The introduction of heterocycles in polymer chains increases their flexibility and makes it easier to optimize the fiber structure. However, the inadequate orientation of polymer chains is one of the main reasons for the large difference between the measured and theoretical mechanical properties of PBIA fibers. Herein, carbon nanotubes (CNTs) are selected as an orientation seed. Their structural features allow CNTs to orient during the spinning process, which can induce an orderly arrangement of polymers and improve the orientation of the fiber microstructure. To ensure the complete 1D topology of long CNTs (≈10 µm), PBIA is used as an efficient dispersant to overcome dispersion challenges. The p-CNT/PBIA fibers (10 µm single-walled carbon nanotube 0.025 wt%) exhibit an increase of 22% in tensile strength and 23% in elongation, with a maximum tensile strength of 7.01 ± 0.31 GPa and a reinforcement efficiency of 893.6. The artificial muscle fabricated using CNT/PBIA fibers exhibits a 34.8% contraction and a 25% lifting of a 2 kg dumbbell, providing a promising paradigm for high-performance organic fibers as high-load smart actuators.

1. Introduction

Poly(p-phenylene-benzimidazole-terephthalamide) (PBIA) fibers, a typical kind of heterocyclic aramid fibers (HAFs), are para-aromatic polyamide fibers with heterocyclic monomers in the polymer chains.[1–3] Aramid fibers are among the world's top three high-performance fibers with high strength, high Young's modulus, lightweight, and high-temperature resistance.[4,5] Because of these properties of aramid fibers, they can endure high dynamic loads and local impact and have therefore been used in various applications in fields such as ballistic protection[6,7] and aerospace.[8] The flexibility of the polymer chains increases with the introduction of heterocyclic monomers, making it easier to adjust the orientation of polymer chains during the spinning process. The improved alignment reduces the defects and stress concentration points caused by the poor orientation of the polymer.[9–11] Therefore, the mechanical properties of PBIA fibers are further improved compared to those of poly(p-phenylene terephthalamide) (PPTA) fibers. However, there is a huge difference between the measured and theoretical mechanical properties of PBIA fibers (tensile strength >30.0 GPa and Young's modulus >182.0 GPa)[1] because of structural defects (concentration of stresses) caused by an inadequate orientation of polymer chains. However, so far,

D. Yan, X. Han, K. Jiao, L. Qian, X. Zhao, J. Zhang
School of Materials Science and Engineering
Peking University
Beijing 100871, China
E-mail: jinzhang@pku.edu.cn

D. Yan, J. Luo, K. Jiao, X. Zhang, Z. Gao, J. Zhang
Beijing Graphene Institute (BGI)
Beijing 100095, China
E-mail: gaozf-cnc@pku.edu.cn

J. Luo, X. Zhang, J. Zhang
Center of Nano Chemistry
Beijing National Laboratory for Molecular Sciences
College of Chemistry and Molecular Engineering
Academy for Advanced Interdisciplinary Studies
Peking University
Beijing 100871, China

The ORCID identification number(s) for the author(s) of this article can be found under https://doi.org/10.1002/adma.202306129

DOI: 10.1002/adma.202306129

S. Wang, Z. Zhang
National Center for Nanoscience and Technology
Beijing 100190, China

X. Lei, X. Wu
Institute of Mechanics
Chinese Academy of Sciences
Beijing 100190, China

X. Lei, X. Wu
School of Engineering Science
University of Chinese Academy of Sciences
Beijing 100049, China

J. Di
Advanced Materials Division
Key Laboratory of Multifunctional Nanomaterials and Smart Systems
Suzhou Institute of Nano-Tech and Nano-Bionics
Chinese Academy of Sciences
Suzhou 215123, China

methods to improve the mechanical properties of PBIA fibers are restricted to adjusting the spinning process and modifying monomers.[3,12–14] The introduction of a 1D material, with a morphology similar to that of polymer chains but more easily oriented, may induce an orderly arrangement of polymers. The 1D material can act as an orientation seed to drive the surrounding polymers to align along the axial direction of the fiber and improve the crystallization and orientation of fibers, increasing their mechanical strength.

Carbon nanotubes (CNTs), especially long CNTs with lengths in the range of micrometers, exhibit a typical 1D topology, ultrahigh intrinsic mechanical properties (tensile strength >100 GPa and Young's modulus >1 TPa), and better rigidity than polymer chains.[15–17] They are more likely to orient along the axial direction during a spinning flow.[18–20] Using this orientation advantage to induce a more efficient orientation of polymer chains can reduce defect points and improve the overall polymer alignment in fibers.[21–23] Therefore, CNTs are the perfect material to use as orientation seeds. This has been verified by our group's previous study on improving the mechanical properties of HAFs using aminated single-walled carbon nanotubes (SWNTs).[24] However, the application of long CNTs is limited by their tendency to tangle and difficult dispersion.[25–28] An excellent dispersion can improve the effective interaction area between the polymers and CNT surface, ensure positive induction, and avoid defect introduction inside fibers.[29–31] The general chemical functionalization dispersion method is widely used to improve the dispersibility of CNTs by introducing functional groups at defective sites on the surface of CNTs.[32,33] However, it is still difficult to unentangle long CNTs and maintain a stable dispersion condition because the number of modification sites is limited.[34,35] Further increasing the functionalization will seriously impair the structural and mechanical properties of CNTs. Therefore, further functionalization is not suitable for the efficient dispersion of long CNTs and will damage the 1D structures of CNTs. Using noncovalent adsorption to uniformly attach polymer chains to the CNT surface to disperse and stabilize long CNTs is preferred because it is not limited by the number of functionalization sites.[36–40]

Herein, PBIA was used to assist the damage-free dispersion of CNTs because the benzene ring structure of PBIA has strong interactions with the surface of CNTs. This dispersion strategy has the following advantages. 1) It affords remarkable dispersion of CNTs with lengths >10 μm in organic solvents. 2) It affords the defect-free surface modification of PBIA on CNTs (p-CNT) and does not damage the intrinsic properties of CNTs. 3) It provides sufficient time and space for the polymer to adjust its orientation during the dispersion process and adsorb onto the surface of CNTs in the lowest energy. The adsorbing layer optimizes the interface between CNTs and polymers and enhances the load transfer efficiency and enhancement efficiency (EE).[41] Finally, 4) it is extremely compatible with the spinning system, and no impurities are introduced. Using this dispersion method, PBIA was in situ polymerized with micrometer-long SWNTs to obtain p-SWNT-enhanced PBIA (p-SWNT/PBIA) fibers via wet spinning (**Figure 1**a). The addition of 10 μm long SWNTs with a weight ratio of 0.025% (0.025 wt%) increases the strength and elongation of the p-SWNT/PBIA fiber by 22% and 23%, respectively, and the dynamic mechanical properties also significantly improve (Figure 1c) after optimization of the polymerization and spinning processes. The strength EE is used to describe the degree of increase in the strength of the fiber because of CNTs and is calculated as follows:

$$\mathrm{EE} = \frac{(\sigma_{\mathrm{E}} - \sigma_{\mathrm{P}})/\sigma_{\mathrm{P}} \times 100\%}{\omega} \tag{1}$$

where σ_{E} is the enhanced strength, σ_{P} is the primary strength, and ω is the mass ratio of CNTs in fibers. The EE of p-SWNT/PBIA (0.025 wt%) up to 893.6 was obtained, much higher than that reported in the literature (Figure 1d). The addition of SWNTs in the fibers reduces the porosity and further improves the crystallization and orientation of the fibers. Full-atom simulations and coarse-grained (CG) simulations were performed to study the enhancement mechanism. An electrothermally driven artificial muscle actuator was prepared using the high-strength and high-toughness p-SWNT/PBIA fibers. The four-ply structure of the artificial muscle exhibits a 34.8% contraction and the combined yarns of 18 artificial muscles can lift a heavy load of up to 2 kg. This artificial muscle with significant strength advantages is a candidate for high-output artificial muscle applications.

2. Results and Discussion

2.1. Strategy for the Efficient and Damage-Free Dispersion of SWNTs

SWNTs exhibit excellent mechanical properties and 1D structures, showing advantages in the field of polymer fiber reinforcement.[20,57,58] However, SWNTs are prone to entanglement and difficult to disperse in various solvents. Their uniform dispersion in the PBIA system is necessary to achieve effective stress transfer and enhance the mechanical properties of fibers.[41] Herein, SWNTs were modified via the noncovalent functionalization of PBIA (p-SWNTs) to improve their dispersion and stability in dimethylacetamide (DMAC)/lithium chloride (LiCl) solvents after considering their dispersion effect and compatibility with the system (**Figure 2**a).

First, the SWNTs were pretreated to ensure the solvent was immersed between the SWNTs to open a channel for the entry of PBIA. Subsequently, under the effect of ultrasonic cavitation, PBIA entered, unentangled, and then was uniformly adsorbed on the surface of SWNTs, preventing their reaggregation and forming a stable SWNT dispersion. When the same operation was performed by directly adding SWNTs into the solvent system, SWNTs were not dispersed. The dispersity of SWNTs is significantly improved by the addition of PBIA (Figure 2b). The morphology of SWNTs in the dispersion was observed using cryogenic transmission electron microscopy (Cryo-TEM; Figure 2c). Figure 2d shows the morphology of polymers adsorbed on the surface of SWNTs. The adsorption of PBIA was studied via energy-dispersive X-ray spectroscopy (Figure S6, Supporting Information). Because the interaction pattern of PBIA on the surface of SWNTs is difficult to characterize, the interaction between PBIA and SWNT was further explored using full-atom simulation calculations.

As shown in Figure 2e, the full-atom models of PBIA and SWNTs were used for molecular dynamics (MD) simulations to

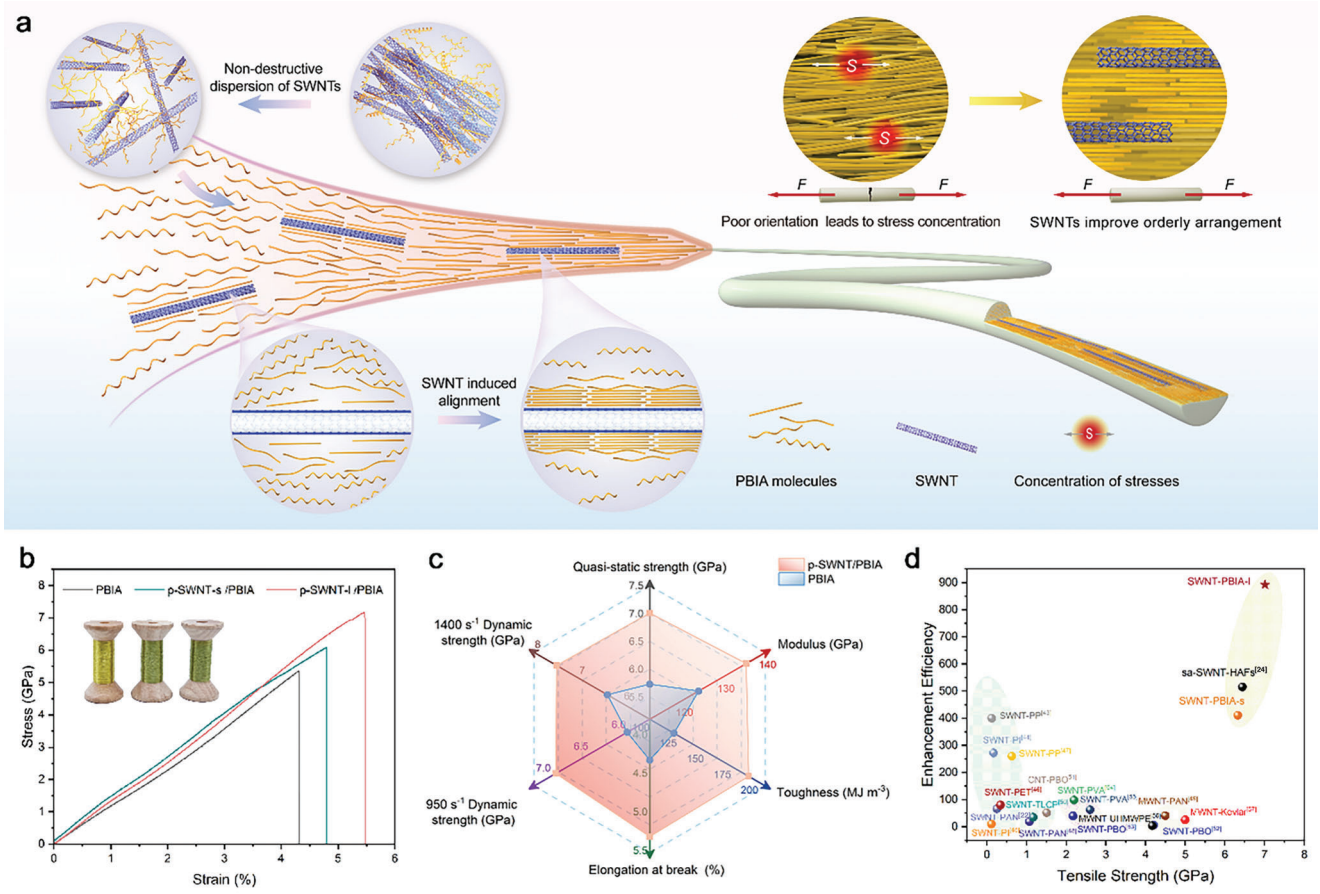

Figure 1. Continuously preparation of p-SWNT-reinforced PBIA fibers. a) Schematic of the wet-spinning process and enhancement mechanisms of p-SWNT/PBIA fiber. b) Stress–strain curves of different fibers [p-SWNT-s/PBIA means fibers with 0.025 wt% short (≈1 μm) SWNTs, p-SWNT-l/PBIA means fibers with 0.025 wt% long (≈10 μm) SWNTs]. c) Comparison of the mechanical performance of p-SWNT/PBIA and PBIA. d) Comparison of EE and tensile strength of different CNT-reinforced organic fibers.[42–56]

study the adsorption mode of PBIA on the SWNT surface. The details of the full-atom MD simulations are given in the Supporting Information. Different dispersion mass ratios of PBIA to SWNT (m_p:m_c) were studied to determine their dispersity in a DMAC/LiCl solution. At a low dispersion ratio, the average distance between two SWNTs is small and the bundling of SWNTs in the dispersion is observed (Figure 2e). Increasing the dispersion ratio improves the dispersion of SWNTs in the solution. However, excessive content of PBIA adsorbed on SWNTs leads to chain clustering. The optimal dispersion ratio of PBIA to SWNT where the best dispersion of SWNTs in solution is achieved is ≈2:1, according to experimental and simulation results.

2.2. Structural Characterization of p-SWNT/PBIA Fibers

The p-SWNT/PBIA fibers with different SWNT contents were obtained via low-temperature polymerization and wet spinning. **Figure 3**a shows the scanning electron microscopy (SEM) image of the p-SWNT/PBIA fibers with an SWNT content of 0.025 wt%. The surface of p-SWNT/PBIA fibers is smooth, and the apparent color of the fiber significantly changes after the addition of SWNTs (Figure S11, Supporting Information). With an increase in the SWNT content, the color of the p-SWNT/PBIA fiber gradually changes from golden-yellow to black. The SWNTs inside the p-SWNT/PBIA fiber are axially aligned along the fiber, as shown in Figure 3b, and the axially cut ultrathin section of the p-SWNT/PBIA fiber has a thickness of 40–50 nm. Focused ion beam (FIB)-SEM was used to measure the porosity of different fibers. There are three main steps to measuring the porosity: 1) continuous laminar imaging, 2) 3D reconstructing using 3D reconstruction software, and 3) counting the number of pores in fibers and calculating the porosity using the software. FIB-SEM data were collected using Crossbeam 550 (Zeiss), with the FIB operating at 300 pA. The detectable range of the pore size is >10 nm. The porosity of the p-SWNT/PBIA fibers is lower than that of pure PBIA fibers (Figure 3c). PBIA fibers undergo double diffusion and multistage stretching in the coagulation bath during the wet spinning process, and the polymer chains gradually orient along the axial direction of the fiber (Figure S11, Supporting Information). Voids are created between the unoriented polymer chains and surrounding other polymer chains, leading to the formation of defect sites within the fiber, which are the origin of fiber fracture. Improving the polymer orientation can reduce the

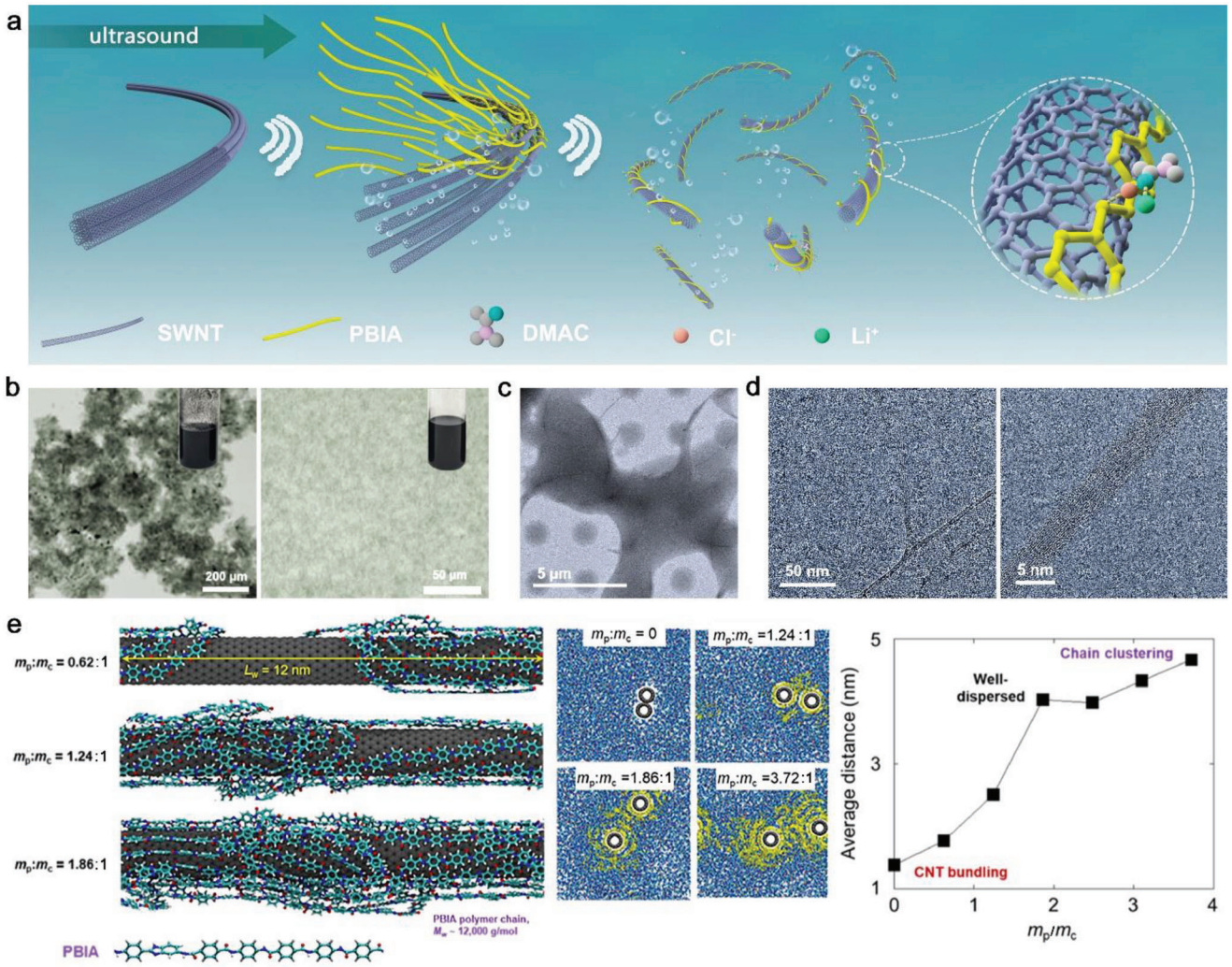

Figure 2. Damage-free dispersion and characterization of p-SWNTs. a) Schematic of the dispersion process of SWNTs via the noncovalent functionalization of PBIA molecules in DMAC/LiCl. b) Optical microscopy images of the SWNT dispersion before (left) and after (right) functionalization by PBIA molecules. The insets are photographs of the corresponding dispersions. c) Cryo-TEM images of the p-SWNT dispersion. d) High Resolution Transmission Electron Microscope (HRTEM) images of the p-SWNT dispersion. e) Simulation calculations of PBIA molecules adsorbed on the SWNT surface and the dispersion ratio of PBIA molecules to SWNTs.

number of defect sites within fibers and improve the mechanical properties of the fiber.[37] Because SWNTs are more easily oriented than polymers during the liquid flow and stretching processes, they are used as orientation seeds during wet spinning; these seeds drive the surrounding polymer chains to rapidly orient along the axis of the fiber, thereby reducing the formation of voids and porosity.

PBIA is a semicrystalline polymer with a lower crystallinity than that of PPTA. The characterization of the crystalline region of the PBIA fibers is particularly difficult and has not yet been reported. Herein, the distribution of SWNTs inside the p-SWNT/PBIA fibers and the lattice of PBIA was studied using ultrathin sections and FIB sections of the p-SWNT/PBIA fibers via spherical-aberration corrected TEM (AC-TEM). The lattice spacing was 4.408 nm (Figure 3d), consistent with the 1D wide-angle X-ray scattering (1D-WAXS) curves from the 2D-WAXS analysis. The lattice fringes of the polymers around the SWNTs align with the orientation of the SWNTs. The different crystalline regions in p-SWNT/PBIA fibers are oriented along the axial direction of the fiber, and the polymers in different amorphous regions are also oriented along the axial direction (Figure S13, Supporting Information). An ≈1.2 nm region near the SWNT shows a clearly ordered transition layer.

The misorientation angle of microfibers was characterized via small-angle X-ray scattering (SAXS). As shown in Figure 3e,f, the misorientation angle decreases with an increase in the content of SWNTs added and the misorientation angle exhibits a minimum value when the SWNT content is 0.025 wt%. Further addition of the SWNTs increases the misorientation angle. The p-SWNT/PBIA fibers with longer (≈10 μm) SWNTs exhibit a smaller misorientation angle because longer SWNTs are easier to orient during the flow process and induce a better orientation and crystallization (Figure S15, Supporting Information).[20] The dispersion ratio of PBIA and SWNTs also affects the

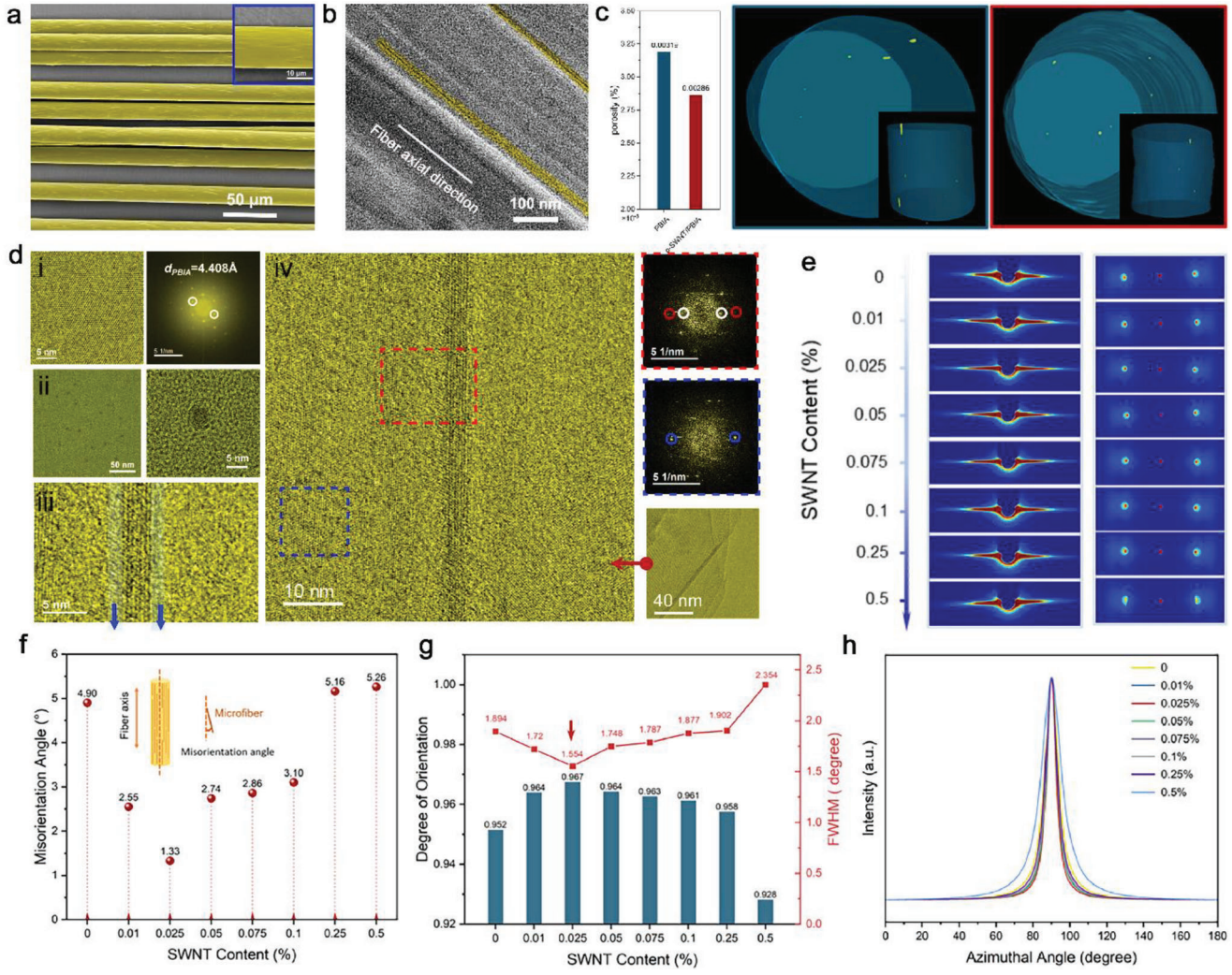

Figure 3. Structural characterization of p-SWNT/PBIA fibers. a) SEM images of p-SWNT/PBIA fibers. b) TEM image of the axial cross-section of the p-SWNT/PBIA fiber. c) Porosity and 3D-reconstructed void microstructure of the PBIA fiber (left) and p-SWNT/PBIA fiber (right) derived from FIB/SEM. d) Spherical AC-TEM images of an ultrathin section in the p-SWNT/PBIA fiber: i) lattice fringe of the p-SWNT/PBIA fiber, ii) cross-section of SWNTs inside the fiber, iii) ordered cladding layer on the surface of SWNTs, and iv) SWNTs and surrounding PBIA lattice fringes. e) 2D-SAXS patterns (left) and 2D-WAXS patterns (right) of p-SWNT/PBIA fibers with different p-SWNT contents. f) Comparison of the microfiber misorientation angle of different fibers derived from 2D-SAXS analysis. g) Comparison of the orientation degree and 1D-WAXS curve FWHMs of different fibers derived from 2D-WAXS analysis. h) Azimuthal intensity profiles of different fibers derived from the 2D-WAXS analysis. The lines were obtained by Lorentz fitting.

misorientation angle of p-SWNT/PBIA microfibers. With an increase in the PBIA content, the dispersibility of SWNTs gradually improves and the surface-ordered layer gradually thickens. As the amount of interaction area between SWNTs and PBIA increases, the induction effect of SWNTs as orientation seeds is further enhanced, which also decreases the misorientation angle of the p-SWNT/PBIA fibers (Figure S15, Supporting Information). When the PBIA content further increases, the ordered layer of polymers adsorbed on the SWNT surface becomes saturated, and excess polymers in the dispersion entangle, which decrease the dispersibility of SWNTs, thereby gradually increasing the misorientation angle.

The crystallinity of the p-SWNT/PBIA fibers was characterized via WAXS. The 2D images (Figure 3e) were integrated to obtain the azimuthal curves and the full width at half-maximum (FWHM) of the p-SWNT/PBIA fibers with different SWNT contents (Figure 3h). The degree of orientation (s) of the crystalline region can be calculated using Equation (1):

$$s = \frac{180 - \mathrm{FWHM}}{180} \tag{2}$$

where the FWHM is the full width at half-maximum of the azimuthal curves. The 1D curve (Figure S16, Supporting Information) was derived by sector integration. The relative size of fiber crystallinity was positively correlated with the FWHM of the 1D curve (Figure 3g). The degree of orientation of the p-SWNT/PBIA fibers increases with an increase in SWNT content, is the maximum at an SWNT content of 0.025 wt%, and then gradually decreases. The FWHM of the 1D curve exhibits the minimum value

at an SWNT content of 0.025 wt%. The narrower the FWHM, the higher the crystallinity of the fiber, indicating that the highest crystallinity is achieved at a 0.025 wt% SWNT content. When the same amount of SWNTs is added, the p-SWNT/PBIA fibers with longer SWNTs exhibit higher orientation factors and better crystallinity (Figure S17, Supporting Information). The best crystalline region's orientation and crystallinity of the p-SWNT/PBIA fibers (Figure S19, Supporting Information) is achieved when the dispersion mass ratio of PBIA and SWNT is 2:1. It indicates that the dispersibility and the ordered layer on the surface of SWNT reached an optimal condition.

2.3. Mechanical Properties of p-SWNT/PBIA Fibers

The mechanical tests directly show that SWNTs improve the mechanical properties of p-SWNT/PBIA fibers. The tensile strength of p-SWNT/PBIA fibers reached a maximum value of 7.01 ± 0.31 GPa at an SWNT addition of 0.025 wt% (10 μm), which was 22% higher than that of pure PBIA fibers of 5.73 ± 0.28 GPa. However, the tensile strength started to decrease with further increase of SWNT content, and was lower than that of pure PBIA fibers when the addition amount exceeded 0.1 wt%. The elastic modulus of p-SWNT/PBIA fibers (137.22 ± 6.53 GPa at SWNT of 0.025 wt%) increased slightly compared with that of pure PBIA fibers (125.76 ± 8.42 GPa), but it did not change significantly at different SWNT additions, and the content of SWNT at 0.5 wt% made the elastic modulus lower than that of pure PBIA fibers. With the increase of SWNT content, the elongation at break of the p-SWNT/PBIA fibers showed a trend of increasing and then decreasing, reaching a maximum at 0.025 wt% (5.32 ± 0.25%), which was 23% higher than that of pure PBIA fibers (4.33 ± 0.24%) (**Figure 4**a,d). The specific strength of a fiber can be used to evaluate the lightweight performance of a fiber. The specific tensile strength and specific modulus of PBIA, p-SWNT-s/PBIA and p-SWNT-l/PBIA monofilaments are shown in Figure S20 in the Supporting Information. The specific strength of the p-SWNT-l/PBIA monofilaments is significantly improved.

This degree of a simultaneous increase in strength and elongation of a high-strength organic fiber is significant and is of great importance for the application of PBIA fibers in fields such as aerospace and ballistic protection. This may be because of several factors. A trace amount of long SWNTs inside the fiber can act as orientation seeds, effectively orienting the polymers and thus improving the crystallinity and orientation degree of the fibers. The effects of the CNT orientation on the mechanical properties of the p-SWNT/PBIA fiber can be considered by two types of contributions: the CNT itself and the polymer near the CNTs. Because the content of the CNTs is very small (0.025 wt%), the major contribution is due to the latter (i.e., the polymer near the CNTs), whose orientation degree and crystallinity are greatly influenced by the CNTs. The tensile strength and Young's modulus can be analytically correlated with the misorientation angle.[59,60] As the SWNT content increases, the higher probability of forming defective spots inside the fiber will create an inhibitory effect on the reinforcement. When the inhibitory effect is greater than the reinforcing effect, the mechanical properties cannot be improved. The EE of p-SWNT/PBIA increases to 893.6, which shows the ultrahigh efficiency of SWNTs in improving the mechanical properties of fibers and shows that small additions of SWNTs can significantly improve the mechanical properties of fibers. It also reflected the advantage of length and dispersion of SWNTs in this work.

On the one hand, SWNTs drive the orderly arrangement of polymer chains to reduce the generation of defective sites inside the fiber and improve the tensile strength of the fiber. On the other hand, because of the more orderly arrangement of polymers, the distance between polymer chains decreases, and the interaction improves, which increases the axial sliding in tension and consequently increases the elongation at break. The degree of the excluded volume of CNTs can be described using a dimensional parameter called the excluded volume potential,[61] $V_{ex} \approx ndl^2 < \sin\varphi >$, where n is the number of CNTs per unit volume, d is the diameter, l is the length, and φ is the misorientation angle. At the same orientation and volume fraction, V_{ex} is scaled with the length (l) in an exponent of 2. The longer CNTs have a greater exclude volume effect. This effect creates a high local concentration of polymer chains, which can help them adsorb onto the CNT surface and entangle with CNTs (Figure 2e). The entanglement of polymer chains with CNTs and the restricted movement of polymer chains near the space occupied by CNTs can form a reinforced network that provides enhanced mechanical properties. Therefore, the addition of an appropriate amount of SWNTs improves the strength and elongation of fibers. For the p-SWNT/PBIA fibers with different SWNT lengths at the same addition, the mechanical properties of the longer SWNTs (≈10 μm) are better than those of the relatively shorter ones (≈1 μm) (Figure 4b,e), consistent with the previous structural characterization results which report that longer SWNTs are more efficient in inducing the orientation of polymers than shorter SWNTs.[62] However, the length of the SWNT is negatively correlated with its dispersibility. The longer the SWNTs, the more difficult to disperse them because they are easier to entangle. Therefore, it is essential to consider all factors when selecting the SWNT length. The mechanical properties of the p-SWNT/PBIA fibers with different polymer and SWNT dispersion ratios also follow a behavior consistent with the structural characterization, and the best mechanical properties are obtained when the dispersion ratio of polymer and SWNTs = 2:1 (Figure 4c,f), attributed to the optimal dispersion and surface-ordered layer of SWNTs. The mechanical properties of fiber yarns can be used to evaluate the application potential of fibers. The mechanical properties of p-SWNT/PBIA fiber yarns (containing 20 fibers) have the same enhancement performance as that of monofilaments (Figure S21, Supporting Information). The test length of fiber yarns was 170 mm, the stretching speed was 25 mm min^{-1}, and the strength was expressed in cN $dtex^{-1}$. The specific tensile strength of p-SWNT/PBIA fiber yarns (SWNT of 10 μm, 0.025 wt%) reaches 37.80 ± 0.98 cN $dtex^{-1}$, while the specific tensile strength of the pure PBIA fiber yarn is 31.05 ± 1.36 cN $dtex^{-1}$.

PBIA fibers are often used as impact-resistant materials in structural components subjected to impact forces,[63] and therefore, dynamic strength at different loading strain rates is important and measured using a mini-split Hopkinson tensile bar (Figure 4g). The dynamic strength of the p-SWNT/PBIA fibers is higher than that of the pure PBIA fibers at loading strain rates of 900 and 1400 s^{-1} (Table S6, Supporting Information).

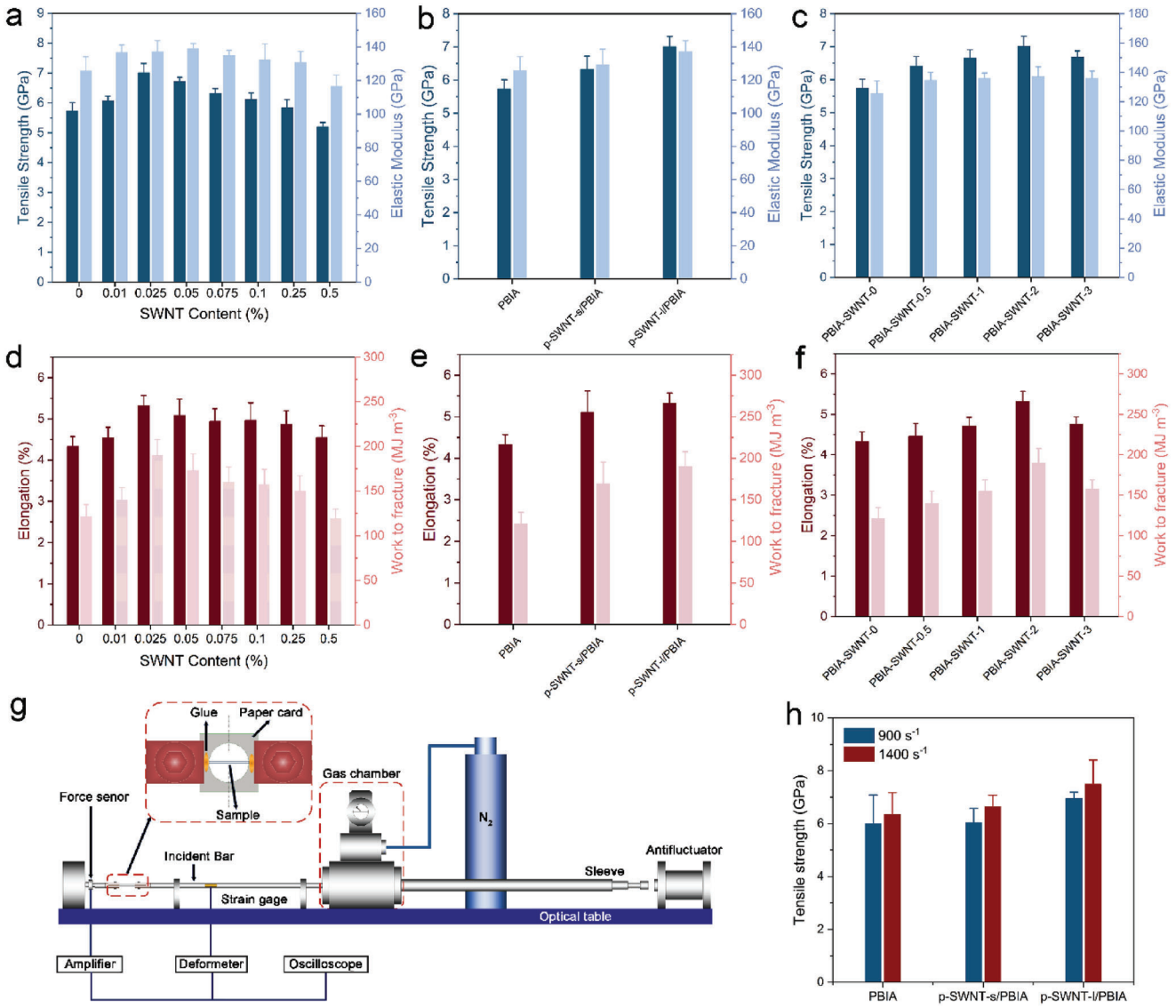

Figure 4. Mechanical properties of different fibers. Comparison of the tensile strength and Young's modulus of p-SWNT/PBIA fibers with different a) SWNT contents, b) SWNT lengths, and c) dispersion ratios of PBIA molecules and SWNTs. Comparison of the elongation and work to fracture of p-SWNT/PBIA fibers with different d) SWNT contents, e) SWNT lengths, and f) dispersion ratios of PBIA molecules and SWNTs. g) Schematic of the dynamic strength test device. h) Dynamic strength comparison of fibers at different loading strain rates.

The dynamic strength increases with an increase in loading strain rates for all fibers (Figure 4h). The p-SWNT/PBIA fibers fabricated using 10 μm SWNT have superior dynamic mechanical properties because they have a better microstructure. The p-SWNT/PBIA fibers are less damaged at fracture than the PBIA fibers (Figure S24, Supporting Information).

In the wet spinning process, the fibers need to be drawn in the secondary solidification bath. The mechanical properties of the fibers are significantly affected by the draw ratio (Figure S22, Supporting Information). The mechanical properties of the fibers substantially improve as the draw ratio increases, which is attributable to the gradual increase in fiber orientation. However, when it exceeds the fiber tolerance, the fiber structure is negatively affected, and defective sites start developing, leading to a decrease in fiber properties. The optimum mechanical properties of the p-SWNT/PBIA fibers are obtained at a draft ratio of 2.3.

2.4. Simulation of p-SWNT/PBIA Fiber Reinforcement Mechanism

The adsorption of PBIA molecules on SWNTs not only improves the dispersity of SWNTs but also increases the interfacial load transfer by enhancing the local structural order of PBIA chains near SWNTs. As shown in **Figure 5**a, the local order parameter,[64] P_i, is calculated for PBIA chains near SWNT (up) and p-SWNT (down), and the details for its calculation are given in

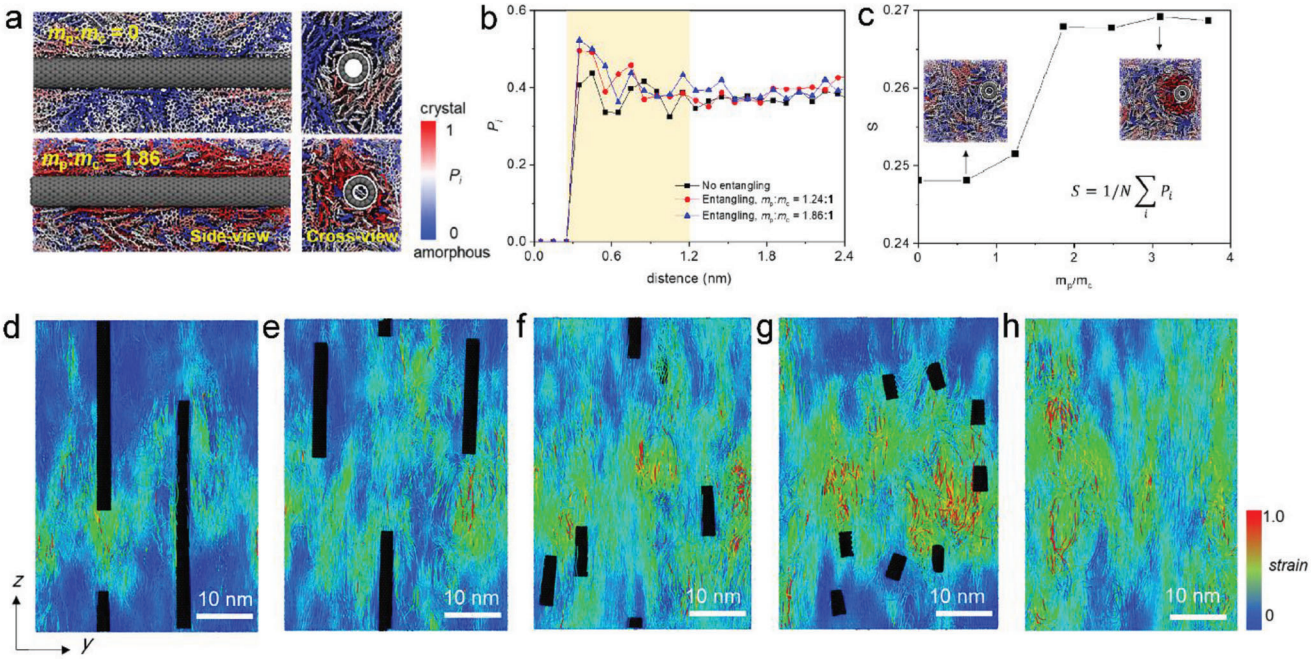

Figure 5. Simulation analysis of p-SWNT/PBIA fibers. a) Local order of PBIA chains near the SWNT (up) and p-SWNT (down). b) Local order of PBIA chains at different distances from the surface of the p-SWNT in different dispersion ratios. c) Global order of PBIA chains near the p-SWNT in different dispersion ratios. The von Mises strain distribution in PBIA chains with different p-SWNT lengths of d) 40 nm, e) 20 nm, f) 8 nm, and g) 4 nm ($\varepsilon_z = 20\%$). h) von Mises strain distribution in PBIA chains without SWNTs.

Supporting Information. The P_i ranges from 0 to 1, corresponding to the amorphous and crystal local structures. As shown in Figure 5b, the case with p-SWNT (m_p: m_c = 1.86:1) demonstrates a more crystal regime near the SWNT than that of the SWNT (m_p: m_c = 0). This result is consistent with the 1.2-nm ordered transition layer near the SWNT observed via TEM. The more crystal regimes of PBIA chains indicate better mechanical performance in terms of strength and Young's modulus, which improves the mechanical properties of the p-SWNT/PBIA fibers. The global structural order of PBIA chains near the p-SWNT at different dispersion ratios is shown in Figure 5c. A critical dispersion ratio for the global order is $\approx m_p:m_c$ = 2:1, which is identical to the dispersion of SWNTs in Figure 2e. This shows that the adsorption of PBIA on the surface of SWNTs is saturated beyond the critical dispersion ratio. The dispersion and crystallinity will not significantly improve by further increasing the number of PBIA molecules on SWNTs.

The use of PBIA molecules adsorption on SWNTs enables us to disperse the long SWNTs in solutions, where the length of SWNTs has impacts on the alignment and load transfer efficiency of PBIA fibers. During the spinning process, longer microfibers usually have a better axial alignment and a larger overlapping between neighboring microfibers.[19] To determine the effects of the length of SWNTs on load transfer, a CG model is proposed to describe the p-SWNT/PBIA fibers under tension. The details of CG simulations are given in the Supporting Information. The von Mises strain distribution in the p-SWNT/PBIA fibers with different SWNT lengths under uniaxial tension (ϵ_z = 20%) is shown in Figure 5d–g. The PBIA chains between the ends of SWNTs indicate a larger von Mises strain than those of the chains near the SWNTs for both the short and long SWNTs. However, the short SWNTs have more ends than the long ones at the same mass fraction, showing that the fibers with short SWNTs possess more mechanically weak regions. Therefore, using long SWNTs affords better mechanical properties than short ones.

2.5. High-Output Artificial Muscle Intelligence Actuator Based on p-SWNT/PBIA Fibers

An artificial muscle is a bionic actuator that imitates the function of skeletal muscles and is inspired by biological muscles but with far superior actuation performance and diversified actuation modes.[65–67] It can produce reversible movements in the form of contraction, rotation, bending, and so forth under external stimulation and has very important applications in simulated robots, prosthetic limbs, flexible exoskeletons, and wearable materials.[68–70] A highly loaded electrothermally driven artificial muscle was fabricated by cotwisting p-SWNT/PBIA fibers with CNT ribbons because of the excellent mechanical properties, weaveability, and thermal expansion of p-SWNT/PBIA fibers.[71–75] The CNT ribbons act as an electrical heat-transfer device to thermally drive the artificial muscle through an applied circuit. The fibers expand and the cross-section generates an untwisting moment, causing the twisted fibers to untwist as the temperature increases. The temperature of the artificial muscle (100 fibers) reached 196.7 °C. An upward contraction of the driven deformation is produced by the polymer untwisting (**Figure 6**a). The artificial muscle return to its initial state as the temperature decreases after the power is turned off. Figure 6b

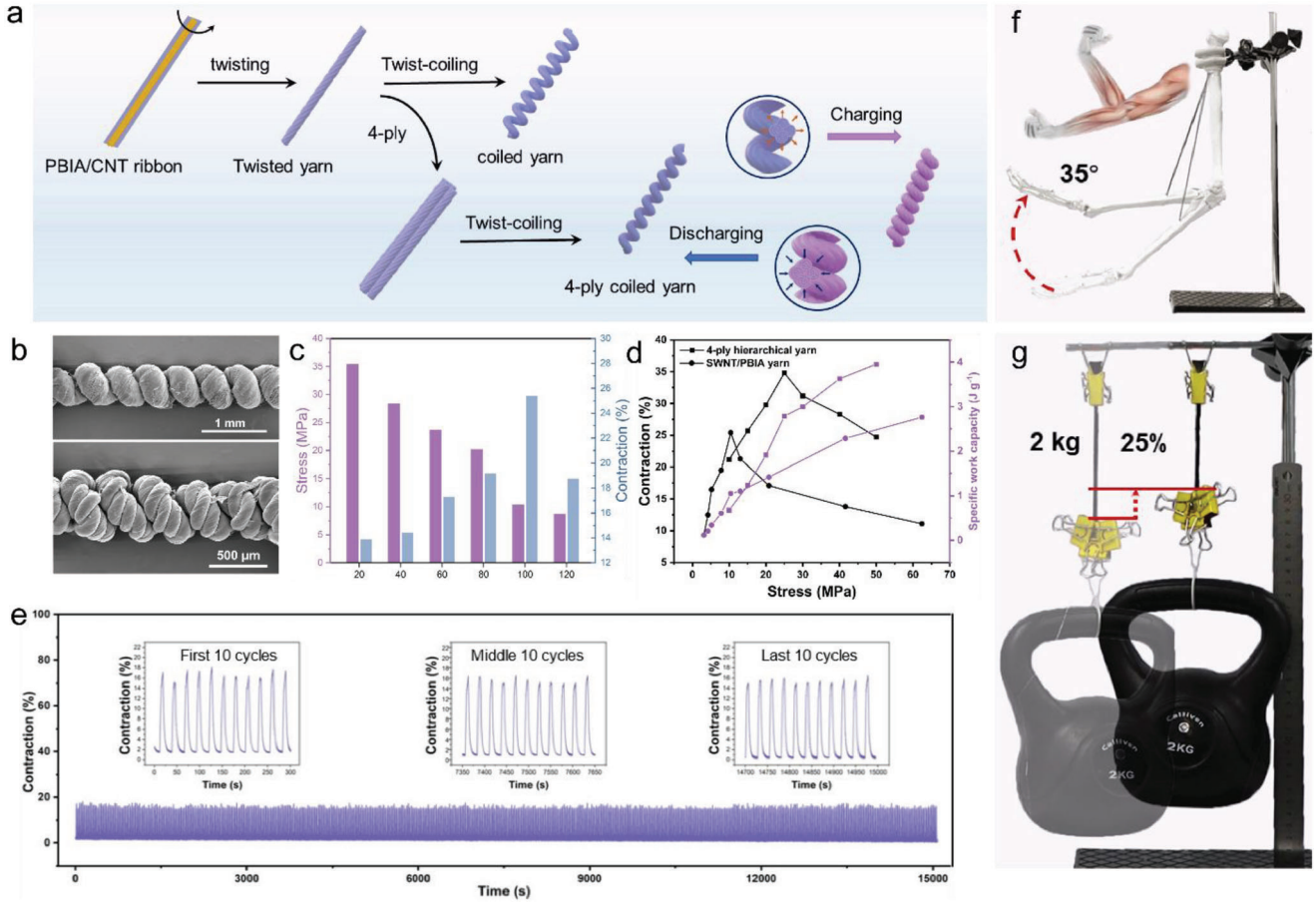

Figure 6. Properties of high-output artificial muscles prepared using p-SWNT/PBIA fibers. a) Schematic of the preparation process and response mechanism of yarn muscles. b) SEM images of single-ply (up) and four-ply (down) p-SWNT/PBIA yarn muscles. c) Stress and contraction of different yarn muscles consisting of different numbers of fibers. d) Contraction and output energy density of single-ply and four-ply p-SWNT/PBIA yarn muscles. e) Cyclic tests of contraction with a real-time path tracing signal (under a 0.12 A current with a 100 g load, powering on for 7 s and powering off for 20 s) on the single-ply p-SWNT/PBIA yarn muscle. The inset shows the first ten cycles, the middle ten cycles, and the last ten cycles of the real-time path tracing signal. f) Schematic and optical image of forearm motion driven by a single-ply p-SWNT/PBIA yarn muscle. g) Optical image of lifting a 2 kg load driven by a single-ply p-SWNT/PBIA yarn muscle.

shows the SEM images of the single-ply twisted artificial muscle and the four-ply twisted artificial muscle, in which the uniform helical structure can be seen. The contraction of artificial muscles prepared using p-SWNT/PBIA fibers with different SWNT contents was tested under different loads. The best performance is achieved with an SWNT content of 0.025 wt% (Figure S31, Supporting Information), which is closely related to the higher internal structural organization of the fiber. Because the monofilaments have the highest strength and work to fracture at this SWNT content, the artificial muscles obtained by twisting exhibit the optimum structure and mechanical properties. The single-ply artificial muscle prepared using 20 fibers exhibits the highest output stress of 35.4 MPa and that prepared using 100 fibers exhibits the highest contraction of 25.4% (Figure 6c). As the number of fibers increases, the thermal expansion volume of the artificial muscle increases, and the contraction shows an upward trend. However, when the number of fibers is too large, it is difficult to evenly twist the entire bundle of fibers, causing defects in the twisting structure and reducing the contraction. As the number of fibers increases, the regularity of the twisted structure decreases, and the increase in cross-sectional area is greater than the increase in load, resulting in lower stress.

The specific work capacity (SWC) of the actuator fibers was calculated as follows:

$$\mathrm{SWC} = \frac{mgh}{M} \tag{3}$$

where m, g, h, and M are the mass of the load, the gravitational acceleration, the height of the lifting load, and the mass of the actuator fibers, respectively. The contraction and output energy density of the artificial muscle increase to 34.8% and 3.96 J g^{-1} when a four-ply twist structure is designed (Figure 6d). The remarkable energy density is because of the light-weight and high-strength properties of the SWNT/PBIA fiber and the optimization of the twisting structure. The artificial muscle exhibits outstanding cyclic stability because of the inherent thermal

stability, high strength, and work to fracture of p-SWNT/PBIA fibers. Figure 6e shows the cycling results of the artificial muscle with 100 fibers. Stable contraction and recovery properties are maintained for more than 15 000 s and the contraction is maintained at 18% (Figure 6e).

To show the actuating performance of the artificial muscle more clearly, the contraction form of animal muscle was simulated. Five single yarns were conjoined to connect the two parts of the arm model at the same scale as an adult human (Figure 6f). The model emulated a human arms lift, accomplishing an apparent rotation of 35°. Additionally, a dumbbell of 2 kg was lifted by cojoining 18 single yarns, generating 25% contraction, which does not decrease after cojoining (Figure 6g). The potential of p-SWNT/PBIA fiber-based artificial muscles for applications in the field of high-load intelligent actuation is well demonstrated.

3. Conclusion

In summary, the noncovalent functionalization of SWNTs using the π–π interactions of PBIA achieves a uniform and stable dispersion of micrometer-sized SWNTs. The 1D topology of SWNTs and their orientation advantage during spinning flow made SWNTs ideal orientation seeds to induce the orientation of polymer chains. p-SWNT/PBIA fibers were fabricated via in situ polymerization of the SWNT dispersion with monomers and wet spinning. The presence of SWNTs in PBIA fibers effectively optimizes their internal structure, including crystallinity, orientation degree, and porosity. The tensile strength of p-SWNT/PBIA fibers (10 μm SWNT 0.025 wt%) increased by 22% with a maximum strength of 7.01 ± 0.31 GPa and elongation at break increased by 23% compared to that of pure PBIA fibers. Simulation calculations and experimental results show that the improvement in mechanical properties was mainly due to three aspects. First, the improved dispersibility of SWNTs increases the amount of the SWNT surface effectively exposed to the polymers. Second, the preferential orientation of SWNTs induces efficient orientation of the polymers and improves the crystallinity and orientation degree of the fiber, reducing the defective sites in fibers. The efficiency of intermolecular load transfer is improved to eliminate stress concentration. Finally, the ordered transition layer on the surface of SWNTs promotes the stress transfer between the polymer and SWNT, and the intrinsic strength of the SWNT can be effectively utilized. Artificial muscle fabricated from p-SWNT/PBIA fibers can achieve a maximum contraction of 34.8% and produce 25% contraction at a 2 kg load. The high strength and smart response properties of the p-SWNT/PBIA fibers are adequately developed to provide innovative strategies for the application of high-performance organic fibers in smart actuation.

4. Experimental Section

Damage-Free Dispersion of SWNTs: For purification of SWNTs, the raw SWNTs were heated at 400 °C for 4 h. The catalyst nanoparticles were removed by refluxing the as-produced SWNTs in 37% HCl for 4 h. The as-purified SWNTs were washed with an abundant amount of water and then vacuum-dried at 200 °C. Purified SWNTs (250 mg) were added to 200 mL of DMAC with 3.5 wt% lithium chloride (LiCl) and sonicated (1080 W, 20 kHz) for 30 min. A PBIA (500 mg) polymerization solution was added to the above solution, and sonication was continued for 30 min and repeated three times, each time with 30 min intervals to lower the temperature. The dispersion was stored in a sealed container.

In Situ Synthesis of PBIA with SWNTs Dispersion: The SWNT/PBIA polymer solution was prepared via a low-temperature polycondensation. The polymerization monomers p-phenylenediamine (PPD) and 2-(4-aminophenyl)−5-aminobenzimidazole (PABZ) were added to the DMAC/LiCl solution and stirred for 30 min. The SWNT dispersion was added to the solution and stirred for 10 min. After lowering the solution temperature to below 10 °C, terephthalyl chloride (TPC) was added and stirred for 1.5 h. The molar ratio of the three monomers is 2:3:5 (n_{PPD}: n_{PABZ}: n_{TPC}). The polymerization solution with a dynamic viscosity of 40 000–60 000 mPas was obtained after the reaction was completed. The color of the polymerization solution varied for different SWNT contents.

Preparation of p-SWNT/PBIA Fibers via Wet Spinning: First, air bubbles were removed from the polymerization solution. Then, the polymerization solution without air bubbles was extruded from the spinneret under vacuum pressure into a primary coagulation bath of 50% DMAC and 50% distilled water with a flow rate of 3.5 m min^{-1}. The polymerization solution was then drawn in a secondary coagulation bath of 20% DMAC and 80% distilled water with a draw ratio of 2.3. The primary fibers were obtained after washing and drying, followed by heat treatment (410 °C, 2 min) under nitrogen protection to obtain the final p-SWNT/PBIA fibers.

Molecular Dynamics Simulations of PBIA with SWNTs in Solution: The full-atom molecular models of PBIA, SWNT, and DMAC molecules were generated for MD simulations. The PBIA chain was randomly replicated with the repeated segments, and the molecular weight was controlled at ≈12 000 g mol^{-1} for each chain. The interatomic interactions followed the optimized potentials for liquid simulations force field.[76] Here, a zigzag (14,0) SWNT was constructed with a length of 12 nm and the interactions within SWNT were described using the adaptive intermolecular reactive empirical bond order potential.[77] The intermolecular interactions were modeled by the van der Waals interaction using Lennard-Jones 12-6 potential. The PBIA chains and SWNT were first relaxed at temperature $T = 400$ K for 2 ns in a simulation box of 12 nm × 12 nm × 12 nm. The SWNT was initially fixed and periodic in the axial direction. After relaxation, the PBIA-entangled SWNT was obtained. Two PBIA-entangled SWNTs and DMAC solvents were placed in the periodic simulation box and further equilibrated at 300 K for 8 ns. The time step was 1 fs. The Langevin thermostat and Berendsen barostat were used for temperature and pressure controls with damping constants of 1 and 100 ps, respectively.

Coarse-Grained Model of p-SWNT/PBIA Fiber: The atoms on PBIA chains and SWNTs were grouped into clusters and represented by CG beads. The length of a PBIA chain was 100 CG beads, corresponding to a molecular weight of ≈12 000 g mol^{-1}. Different lengths of SWNTs (4, 8, 20, and 40 nm) were used. 8000 PBIA chains and 40–4 SWNTs were generated in a simulation box under periodic boundary conditions. The mass fraction of SWNTs was ≈0.5%. The initial configuration was relaxed for 5 ns at a temperature of 600 K and then equilibrated at 300 K for 2 ns. The pressure was 1 atm. The Berendsen thermostat and barostat were used for temperature and pressure control with damping-time constants of 1 and 100 ps, respectively. The time step was 1 fs. After relaxation, the box was stretched in the axial direction by up to 20% with a strain rate of 108 s^{-1}. All full-atom MD and Coarse-Grained Molecular Dynamics (CGMD) simulations were implemented using the large-scale atomic/molecular massively parallel simulator.[78]

Preparation of an Artificial Muscle from p-SWNT/PBIA Fibers: A 40-cm CNT ribbon and a certain number of p-SWNT/PBIA fibers were clamped to the motor at one end and a weight of 20–50 g was suspended at the other end. A single yarn was twisted at 125 rpm to produce a uniform spiral structure. 20 fibers and CNT ribbon were cotwisted under a 20 g load until a helix was created. Four twisted yarns were utilized as the component yarns for preparing four-ply yarns. Four of the above yarns were straightened and twisted under an 80 g load at 125 rpm until a uniform

spiral structure was formed. Before testing the actuator fiber, the coiled yarn was driven multiple times with a current of 0.12 A under a load of 10 MPa to fix its shape.

Supporting Information

Supporting Information is available from the Wiley Online Library or from the author.

Acknowledgements

This work was financially supported by the Ministry of Science and Technology of the People's Republic of China (2016YFA0200100 and 2018YFA0703502), the National Natural Science Foundation of China (Grant Nos. T2188101, 52021006, 51720105003, 21790052, 21974004, and 5210020884), the National Natural Science Foundation of China (Grant No. 52102035), the Strategic Priority Research Program of CAS (XDB36030100), and the Beijing National Laboratory for Molecular Sciences (BNLMS-CXTD-202001). Thanks to the beamline BL19U2 of National Centre for Protein Science Shanghai at Shanghai Synchrotron Radiation Facility in conducting the SAXS characterizations. The authors thank Qing Zhang for conducting the WAXS characterizations. The authors are grateful for the technical support of WAXS measurement for Nano-X from Suzhou Institute of Nano-Tech and Nano-Bionics, Chinese Academy of Sciences.

Conflict of Interest

The authors declare no conflict of interest.

Author Contributions

D.Y., J.L., and S.W. contributed equally to this work. J.Z. and Z.G. conceived and supervised the project. D.Y. and J.L. performed the preparation of fibers, with assistance from S.W. performed the theoretical calculations and simulations, with assistance from Z.Z. X.H. performed TEM tests with the help of X.Z. X.L. performed dynamic mechanical tests, with assistance from X.W. All authors contributed to discussions and commented on the paper.

Data Availability Statement

The data that support the findings of this study are available from the corresponding author upon reasonable request.

Keywords

1D topology, artificial muscles, carbon nanotubes, damage-free dispersion, heterocyclic aramid fibers, mechanical properties, orientation seed

Received: June 25, 2023
Revised: July 20, 2023
Published online:

[1] J. Li, Y. Wen, Z. Xiao, S. Wang, L. Zhong, T. Li, K. Jiao, L. Li, J. Luo, Z. Gao, S. Li, Z. Zhang, J. Zhang, *Adv. Funct. Mater.* **2022**, *32*, 2200937.
[2] L. Luo, Y. Wang, Y. Dai, Y. Yuan, C. Meng, Z. Cheng, X. Wang, X. Liu, *J. Mater. Sci.* **2018**, *53*, 13291.
[3] R. Xu, Y. Qiu, S. Tang, C. Yang, Y. Dai, D. Zhang, Y. Gao, K. Gao, L. Luo, X. Liu, *Macromol. Mater. Eng.* **2021**, *306*, 2000814.
[4] L. Penn, F. Milanovich, *Polymer* **1979**, *20*, 31.
[5] M. G. Dobb, D. J. Johnson, B. P. Saville, *Polymer* **1981**, *22*, 960.
[6] Y. S. Lee, E. D. Wetzel, N. J. Wagner, *J. Mater. Sci.* **2003**, *38*, 2825.
[7] T. J. Singh, S. Samanta, *Mater. Today: Proc.* **2015**, *2*, 1381.
[8] G. Lubin, S. J. Dastin, *Handbook of Composites*, Springer, Boston, MA **1982**.
[9] G. Qi, B. Zhang, S. Du, *Composites, Part A* **2018**, *112*, 549.
[10] X. Ding, H. Kong, M. Qiao, Z. Hu, M. Yu, *Polymers* **2019**, *11*, 856.
[11] C. Chen, X. Wang, F. Wang, T. Peng, *J. Macromol. Sci. Part B: Phys.* **2020**, *59*, 90.
[12] C. Yang, H. Wu, Y. Dai, D. Zhang, R. Xu, L. Luo, X. Liu, *Composites, Part B* **2020**, *202*, 108411.
[13] Z. Cheng, X. Li, J. Lv, Y. Liu, X. Liu, *Appl. Surf. Sci.* **2021**, *544*, 148935.
[14] Y. Dai, Y. Yuan, L. Luo, X. Liu, *Composites, Part A* **2018**, *113*, 233.
[15] X. M. Sun, H. Sun, H. P. Li, H. S. Peng, *Adv. Mater.* **2013**, *25*, 5153.
[16] J. N. Coleman, U. Khan, W. J. Blau, Y. K. Gun'ko, *Carbon* **2006**, *44*, 1624.
[17] Z. Spitalsky, D. Tasis, K. Papagelis, C. Galiotis, *Prog. Polym. Sci.* **2010**, *35*, 357.
[18] G. C. Han, M. L. Minus, S. Kumar, *Polymer* **2006**, *47*, 3494.
[19] E. Gao, S. Wang, C. Duan, Z. Xu, *Sci. China: Technol. Sci.* **2019**, *62*, 1545.
[20] S. Zhang, Y. Ma, L. Suresh, A. Hao, M. Bick, S. C. Tan, J. Chen, *ACS Nano* **2020**, *14*, 9282.
[21] S. Zhang, M. L. Minus, L. Zhu, C. P. Wong, S. Kumar, *Polymer* **2008**, *49*, 1356.
[22] G. M. Spinks, V. Mottaghitalab, M. Bahrami-Samani, P. G. Whitten, G. G. Wallace, *Adv. Mater.* **2006**, *18*, 637.
[23] F. M. Blighe, K. Young, J. J. Vilatela, A. H. Windle, I. A. Kinloch, L. Deng, R. J. Young, J. N. Coleman, *Adv. Funct. Mater.* **2011**, *21*, 364.
[24] J. Luo, Y. Wen, X. Jia, X. Lei, Z. Gao, M. Jian, Z. Xiao, L. Li, J. Zhang, T. Li, H. Dong, X. Wu, E. Gao, K. Jiao, J. Zhang, *Nat. Commun.* **2023**, *14*, 3019.
[25] J. P. Salvetat, G. A. D. Briggs, J. M. Bonard, R. R. Bacsa, A. J. Kulik, T. Stöckli, N. A. Burnham, L. Forró, *Phys. Rev. Lett.* **1999**, *82*, 944.
[26] C. Pramanik, J. R. Gissinger, S. Kumar, H. Heinz, *ACS Nano* **2017**, *11*, 12805.
[27] I. A. Kinloch, J. Suhr, J. Lou, R. J. Young, P. M. Ajayan, *Science* **2018**, *362*, 547.
[28] S. W. Kim, T. Kim, Y. S. Kim, H. S. Choi, H. J. Lim, S. J. Yang, C. R. Park, *Carbon* **2012**, *50*, 3.
[29] D. G. Papageorgiou, Z. Li, M. Liu, I. A. Kinloch, R. J. Young, *Nanoscale* **2020**, *12*, 2228.
[30] A. A. Mamedov, N. A. Kotov, M. Prato, D. M. Guldi, J. P. Wicksted, A. Hirsch, *Nat. Mater.* **2002**, *1*, 190.
[31] L. Gong, I. A. Kinloch, R. J. Young, I. Riaz, R. Jalil, K. S. Novoselov, *Adv. Mater.* **2010**, *22*, 2694.
[32] S. T. R. Naqvi, T. Rasheed, D. Hussain, M. Najam ul Haq, S. Majeed, S. shafi, N. Ahmed, R. Nawaz, *J. Mol. Liq.* **2020**, *297*, 111919.
[33] M. Holzinger, O. Vostrowsky, A. Hirsch, F. Hennrich, M. Kappes, R. Weiss, F. Jellen, *Angew. Chem., Int. Ed.* **2001**, *40*, 4002.
[34] P. C. Ma, N. A. Siddiqui, G. Marom, J. K. Kim, *Composite, Part A* **2010**, *41*, 1345.
[35] A. Hirsch, *Angew. Chem., Int. Ed.* **2002**, *41*, 1853.
[36] S. K. Samanta, M. Fritsch, U. Scherf, W. Gomulya, S. Z. Bisri, M. A. Loi, *Acc. Chem. Res.* **2014**, *47*, 2446.
[37] H. D. Lee, B. M. Yoo, T. H. Lee, H. B. Park, *J. Colloid Interface Sci.* **2018**, *509*, 307.
[38] C. Kanimozhi, M. J. Shea, J. Ko, W. Wei, P. Huang, M. S. Arnold, P. Gopalan, *Macromolecules* **2019**, *52*, 4278.
[39] T. Gegenhuber, A. H. Gröschel, T. I. Löbling, M. Drechsler, S. Ehlert, S. Förster, H. Schmalz, *Macromolecules* **2015**, *48*, 1767.

[40] P. J. Arias-Monje, A. A. Bakhtiary Davijani, M. Lu, J. Ramachandran, M. H. Kirmani, S. Kumar, *ACS Appl. Nano Mater.* **2020**, *3*, 4178.
[41] Z. Jiang, F. Wang, J. Yin, S. Gong, Z. Dai, Y. Pang, Y. Xiong, Z. Zhu, Z. Li, *Composite, Part B* **2020**, *199*, 108266.
[42] M. V. Jose, D. Dean, J. Tyner, G. Price, E. Nyairo, *J. Appl. Polym. Sci.* **2007**, *103*, 3844.
[43] S. Chatterjee, F. A. Nüesch, B. T. T. Chu, *Chem. Phys. Lett.* **2013**, *557*, 92.
[44] E. J. Siochi, D. C. Working, C. Park, P. T. Lillehei, J. H. Rouse, C. C. Topping, A. R. Bhattacharyya, S. Kumar, *Composites, Part B* **2004**, *35*, 439.
[45] K. A. Anand, T. S. Jose, U. S. Agarwal, T. V. Sreekumar, B. Banwari, R. Joseph, *Int. J. Polym. Mater.* **2010**, *59*, 438.
[46] G. W. Lee, S. Jagannathan, H. G. Chae, M. L. Minus, S. Kumar, *Polymer* **2008**, *49*, 1831.
[47] H. G. Chae, M. L. Minus, S. Kumar, *Polymer* **2006**, *47*, 3494.
[48] H. G. Chae, Y. H. Choi, M. L. Minus, S. Kumar, *Compos. Sci. Technol.* **2009**, *69*, 406.
[49] Y. Tang, L. Fang, P. Gao, *J. Mater. Sci.* **2012**, *47*, 8094.
[50] Z. Hu, J. Li, P. Y. Tang, D. L. Li, Y. J. Song, Y. W. Li, L. Zhao, C. Y. Li, Y. D. Huang, *J. Mater. Chem.* **2012**, *22*, 19863.
[51] S. Kumar, T. D. Dang, F. E. Arnold, A. R. Bhattacharyya, B. G. Min, X. Zhang, R. A. Vaia, C. Park, W. W. Adams, R. H. Hauge, R. E. Smalley, S. Ramesh, P. A. Willis, *Macromolecules* **2002**, *35*, 9039.
[52] C. Zhou, S. Wang, Y. Zhang, Q. Zhuang, Z. Han, *Polymer* **2008**, *49*, 2520.
[53] X. Xu, A. J. Uddin, K. Aoki, Y. Gotoh, T. Saito, M. Yumura, *Carbon* **2010**, *48*, 1977.
[54] M. L. Minus, H. G. Chae, S. Kumar, *Macromol. Chem. Phys.* **2009**, *210*, 1799.
[55] S. Ruan, P. Gao, T. X. Yu, *Polymer* **2006**, *47*, 1604.
[56] I. O'Connor, H. Hayden, J. N. Coleman, Y. K. Gun'ko, *Small* **2009**, *5*, 466.
[57] Y. Liu, S. Kumar, *ACS Appl. Mater. Interfaces* **2014**, *6*, 6069.
[58] S. G. Kim, S. J. Heo, J. G. Kim, S. O. Kim, D. Lee, M. Kim, N. D. Kim, D. Y. Kim, J. Y. Hwang, H. G. Chae, B. C. Ku, *Adv. Sci.* **2022**, *9*, 2203008.
[59] J. C. Fernández-Toribio, B. Alemán, Á. Ridruejo, J. J. Vilatela, *Carbon* **2018**, *133*, 44.
[60] M. G. Northolt, P. den Decker, S. J. Picken, J. J. M. Baltussen, R. Schlatmann, *Adv. Polym. Sci.* **2005**, *178*, https://doi.org/10.1007/b104207.
[61] G. M. Choi, H. S. Lee, *Macromolecules* **2022**, *55*, 9196.
[62] T. H. Hsieh, Y. S. Huang, M. Y. Shen, *Polym. Compos.* **2018**, *39*, E1072 .
[63] H. Zhou, K. Jiao, *Acta Phys.-Chim. Sin.* **2022**, *38*, 141.
[64] I. C. Yeh, J. W. Andzelm, G. C. Rutledge, *Macromolecules* **2015**, *48*, 4228.
[65] G. V. Stoychev, L. Ionov, *ACS Appl. Mater. Interfaces* **2016**, *8*, 24281.
[66] S. M. Mirvakili, I. W. Hunter, *Adv. Mater.* **2018**, *30*, 1704407.
[67] G. M. Spinks, *Adv. Mater.* **2020**, *32*, 1904093.
[68] L. Dong, M. Ren, Y. Wang, J. Qiao, Y. Wu, J. He, X. Wei, J. Di, Q. Li, *Mater. Horiz.* **2021**, *8*, 2541.
[69] Y. Sun, K. Hou, D. Zhang, S. Chang, L. Ye, A. Cao, Y. Shang, *Compos. Sci. Technol.* **2021**, *206*, 108676.
[70] Y. Y. Wen, M. Ren, J. T. Di, J. Zhang, *Acta Phys.-Chim. Sin.* **2022**, *38*, 2107006.
[71] C. S. Haines, M. D. Lima, N. Li, G. M. Spinks, J. Foroughi, J. D. Madden, S. H. Kim, S. Fang, M. Jung de Andrade, F. Göktepe, O. Göktepe, S. M. Mirvakili, S. Naficy, X. Lepró, J. Oh, M. E. Kozlov, S. J. Kim, X. Xu, B. J. Swedlove, G. G. Wallace, R. H. Baughman, *Science* **2014**, *343*, 868.
[72] H. Chu, X. Hu, Z. Wang, J. Mu, N. Li, X. Zhou, S. Fang, C. S. Haines, J. W. Park, S. Qin, N. Yuan, J. Xu, S. Tawfick, H. Kim, P. Conlin, M. Cho, K. Cho, J. Oh, S. Nielsen, K. A. Alberto, J. M. Razal, J. Foroughi, G. M. Spinks, S. J. Kim, J. Ding, J. Leng, R. H. Baughman, *Science* **2021**, *371*, 494.
[73] J. Mu, M. Jung de Andrade, S. Fang, X. Wang, E. Gao, N. Li, S. H. Kim, H. Wang, C. Hou, Q. Zhang, M. Zhu, D. Qian, H. Lu, D. Kongahage, S. Talebian, J. Foroughi, G. Spinks, H. Kim, T. H. Ware, H. J. Sim, D. Y. Lee, Y. Jang, S. J. Kim, R. H. Baughman, *Science* **2019**, *365*, 150.
[74] S. Tawfick, Y. Tang, *Science* **2019**, *365*, 125.
[75] M. Kanik, S. Orguc, G. Varnavides, J. Kim, T. Benavides, D. Gonzalez, T. Akintilo, C. C. Tasan, A. P. Chandrakasan, Y. Fink, P. Anikeeva, *Science* **2019**, *365*, 145.
[76] W. L. Jorgensen, D. S. Maxwell, J. Tirado-Rives, *J. Am. Chem. Soc.* **1996**, *118*, 11225.
[77] S. J. Stuart, A. B. Tutein, J. A. Harrison, *J. Chem. Phys.* **2000**, *112*, 6472.
[78] S. Plimpton, *J. Comput. Phys.* **1995**, *117*, 1.